Optimizing laser weldability of heat-treatable and non-heat-treatable aluminum alloys: a comprehensive study

Jean-Denis Béguin, Yannick Balcaen, Jade Pécune, Nathalie Aubazac, Joël Alexis

Journal of
Manufacturing and Materials Processing

MDPI

Article

Optimizing Laser Weldability of Heat-Treatable and Non-Heat-Treatable Aluminum Alloys: A Comprehensive Study

Jean-Denis Béguin, Yannick Balcaen, Jade Pécune, Nathalie Aubazac and Joël Alexis *

Université de Toulouse, UTTOP, LGP, 47 Av. d'Azereix, 65016 Tarbes, France; jean-denis.beguin@uttop.fr (J.-D.B.); yannick.balcaen@uttop.fr (Y.B.); jade.pecune@uttop.fr (J.P.); nathalie.aubazac@uttop.fr (N.A.)
* Correspondence: joel.alexis@uttop.fr; Tel.: +33-5-62-44-27-07

Abstract

Laser welding, a vital process in modern industry, offers significant technical and economic benefits, including improved part quality, precision, productivity, and cost reduction. This study significantly enhances our understanding of heat-treatable weldability (AA2024, AA2017, AA6061) and non-heat-treatable AA5083 aluminum alloys. It establishes a "weldability window" based on power density and interaction time, identifying three key domains: insufficient penetration, full penetration with regular weld, and irregular weld or cutoff. The study's findings reveal that heat-treatable alloys soften in the fusion zone due to the dissolution of reinforcing precipitates during welding. In contrast, non-heat-treatable alloys exhibit hardening due to a fine dendritic microstructure. The fusion zone features fine dendrites, and in the heat-affected zone (HAZ), coarse particles and liquation at the fusion line are observed, particularly in AA6061 and 2024 alloys. The study also shows that the joint efficiency, a measure of the weld's load-bearing capacity, is approximately 90% for the AA5083 alloy and 80% for the heat-treatable alloys. These findings significantly contribute to our understanding of welding processes. They can be used to optimize laser welding processes, thereby ensuring the production of high-quality and reliable joints in industrial applications.

Keywords: laser welding; aluminum alloy; aluminum weldability; microstructure; mechanical properties

Academic Editor: Dulce Maria Rodrigues

Received: 26 April 2025
Revised: 25 July 2025
Accepted: 31 July 2025
Published: 25 August 2025

Citation: Béguin, J.-D.; Balcaen, Y.; Pécune, J.; Aubazac, N.; Alexis, J. Optimizing Laser Weldability of Heat-Treatable and Non-Heat-Treatable Aluminum Alloys: A Comprehensive Study. *J. Manuf. Mater. Process.* **2025**, *9*, 290. https://doi.org/10.3390/jmmp9090290

1. Introduction

Laser welding is a rapid and accurate process of joining thin metal sheets without filler metal to reduce weight and cost in the automotive and aeronautical industries [1–5]. It is a satisfactory technique for controlling heat input and, as a consequence, minimizing thermal distortions [6–8].

However, aluminum alloys are difficult to weld because of surface reflectivity and high thermal conductivity [1,3], which can favor a lack of penetration and promote a thermal gradient that can induce thermomechanical stresses [9]. Other problems in welding these alloys are due to the low vaporization temperature of alloying elements such as Mg [10,11], which leads to unstable keyhole processes and porosity formation. On the other hand, some common defects, such as hot cracking and liquation, have been reported, which lead to the degradation of mechanical properties [6,10–12].

Many recent studies and developments have been performed to improve aluminum alloys' weld quality [6]. Most investigations are based on controlling the thermal cycle to prevent hot cracking. Some experiments followed the approach of the type of laser source,

such as CO_2, Yb: fiber continuous [13–15], or Nd: YAG pulsed, [10,16–18]; other kinds of energy distribution [11,19]; or the approach of oscillating [1] and triple-spot optics to improve weld microstructure and reduce porosity [12].

Recent innovations in the laser process have led to the development of a high-power Yb: YAG disc source and 2-1 fiber with high beam quality, which can produce deep penetration welds and reduce porosity formation [20].

This study focuses on the "weldability domain" for different series of aluminum alloys with a Yb: YAG disc source and aims to provide practical insights into the influence of the process parameters on the weld defects. The obtained welds are categorized according to the top weld appearance, geometrical characteristics, and full penetration, with the final mechanical and microstructural properties correlated with the welding process.

2. Materials and Methods

2.1. Materials

Heat-treatable and non-heat-treatable aluminum alloy sheets with a thickness of 1.2 mm were investigated in this work. Two AA2024 Alclad-T3 and AA2017A-T4 alloys were investigated for the 2XXX series, and AA5083-H111 and AA6061-T6 aluminum alloys were investigated for the 5XXX and 6XXX series. The average chemical composition of the aluminum sheets studied is determined using an Oxford-Cegelec FOUNDRY-MASTER spark OES spectrometer (Table 1).

Table 1. Average chemical composition of aluminum alloy sheets (in wt%).

	Mg	Si	Cu	Fe	Mn	Zn	Cr	Ti	Al
AA2017-T4	0.69 ± 0.01	0.62 ± 0.01	4.35 ± 0.03	0.32 ± 0.04	0.64 ± 0.006	0.17 ± 0.002	0.02 ± 0.001	0.05 ± 0.002	Bal.
AA2024-T3	1.36 ± 0.07	0.07 ± 0.002	4.29 ± 0.06	0.11 ± 0.002	0.39 ± 0.005	0.05 ± 0.002	0.0039 ± 0.0003	0.03 ± 0.002	Bal.
AA5083-H111	3.99 ± 0.08	0.20 ± 0.004	0.04 ± 0.003	0.20 ± 0.003	0.39 ± 0.008	0.01 ± 0.001	0.09 ± 0.002	0.01 ± 0.001	Bal.
AA6061-T6	0.8 ± 0.01	0.72 ± 0.01	0.20 ± 0.005	0.44 ± 0.01	0.10 ± 0.001	0.03 ± 0.001	0.02 ± 0.002	0.06 ± 0.002	Bal.

The chemical composition greatly influences the physical properties of aluminum alloys, such as the solidification range and thermal conductivity. The values for the alloys studied are reported in Table 2.

Table 2. Melting range and thermal conductivity of aluminum alloys [21–23].

	Melting Range (°C)	Thermal Conductivity (in W/m. K) at 25 °C
AA2017-T4	535–645	138
AA2024-T3	502–638	120
AA5083-H111	570–638	120
AA6061-T6	582–652	167

Alloys with a wide solidification range and high thermal conductivity are more susceptible to hot cracking [6]. Precipitation-hardened alloys (AA2024 and AA2017) exhibit relatively low thermal conductivity and wide solidification ranges, which increase their tendency toward hot cracking. In contrast, AA5083, a non-heat-treatable Al–Mg alloy, and AA6061, a medium-strength heat-treatable alloy with a narrower solidification range and higher thermal conductivity, are less prone to hot cracking under similar welding conditions. The initial microstructure of wrought aluminum alloys consists of moderately

elongated grains with insoluble coarse particles. These particles have a variable chemical composition as a function of aluminum series and heat treatment: (Cu_2MnAl_{20}, Cu_2FeA_{l7}) for 2XXX series, ($MnAl_6$, Mg_2Si) for 5XXX, and Mg_2Si for 6XXX series. For heat-treatable alloys, a fine hardening precipitate of $CuAl_2$(Mg) for 2XXX (T3 or T4) and Mg_2Si for 6XXX (T6) series is present.

2.2. Welding Methodology and Parameters

Aluminum sheets are cut by laser processing to ensure a precise edge for butt joint configuration welding. After cutting, weld plates of 150 × 32 mm and 130 × 32 mm are mechanically polished with a P600 emery paper to eliminate superficial oxides before welding and cleaned with alcohol.

Plates are mounted in a precise fixture to ensure correct alignment and an accurate laser focus position relative to the joint. A trailing shield and a gas chamber with a gas flow protect the top and root of the weld. Figure 1 shows the experimental procedure scheme, with details of the welding fixture and the geometry of the tensile specimen.

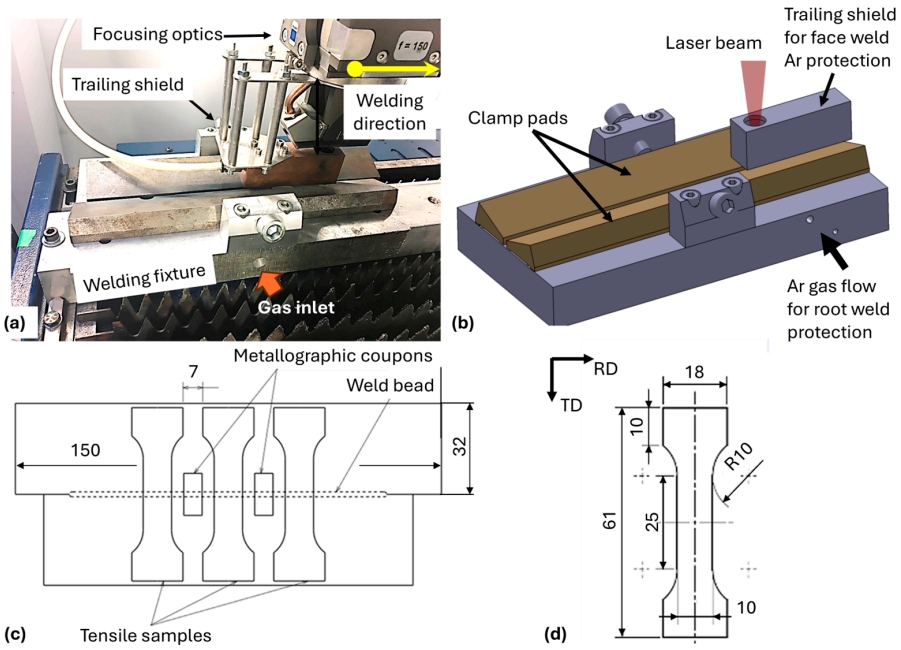

Figure 1. (**a**) Experimental configuration, (**b**) scheme of the laser welding fixture for the butt welding configuration, (**c**) welding scheme concerning the rolling direction and localization of tensile test samples, (**d**) geometry and dimensions of a tensile test specimen.

The laser source used in this study is a continuous Yb: YAG laser disk (TRUMPF SARL, TruDisk 3001, Paris, France) with a maximum power of 3 kW, an emission wavelength of 1030 nm, and a beam parameter product (BPP) of 8 mrad. The delivery fiber core diameter is 100 µm. The optical device provides a broad range of beam diameters of 120 µm to 370 µm. The beam profiler (PRECITEC, FocusMonitor PRIMES, Le Creusot, France) measures the intensity distribution and displays a Gaussian-like distribution at the focus point.

Table 3 lists the experimental parameters considered in determining the weldability window. The focus point is a constant 0.3 mm below the specimen surface for better process stability.

To normalize the effect of power, welding velocity, and focal diameter, combined parameters such as heat input (H), power density (I), and interaction time (τ) are calculated as follows:

$$H = \frac{P}{V} \quad (1)$$

$$I = \frac{P}{S} \quad (2)$$

$$\tau = \frac{\varnothing}{V} \quad (3)$$

P represents the laser power, S is the spot area, ∅ is the spot laser diameter, and v is the welding velocity. From parameters I and t, the energy density (F) can be deduced as follows:

$$F = I \times \tau \quad (4)$$

Table 3. Laser welding parameters and weld characterization.

Welding Parameters	Values	Responses
Power [W]	2500–2700 (3 levels)	Visual aspect
Speed [m/min]	1–13 (7 levels)	Weld penetration
Focal spot diameter [µm]	133–586 (7 levels)	Weld geometry
Argon gas flow [L/min]	40 (top); 20 (bottom)	Tensile test

2.3. Weld Characterization Methods and Equipment

Metallographic specimens for optical examination and tensile tests are cut by laser transversely from the weld area of interest to ensure a comprehensive study of the welds. The top and bottom surfaces of weld seams are analyzed to classify welds according to their morphological characteristics, such as penetration or weld appearance (Figure 2). Optical examination of the cross-section using an OLYMPUS-PMG3 microscope enables analysis of the morphology, macro-, and microstructure of the weld beads to determine weld quality. Geometric defects such as underfill, undercut, and undesirable root profiles are evaluated according to NF-L06-395-2010 specifications [24].

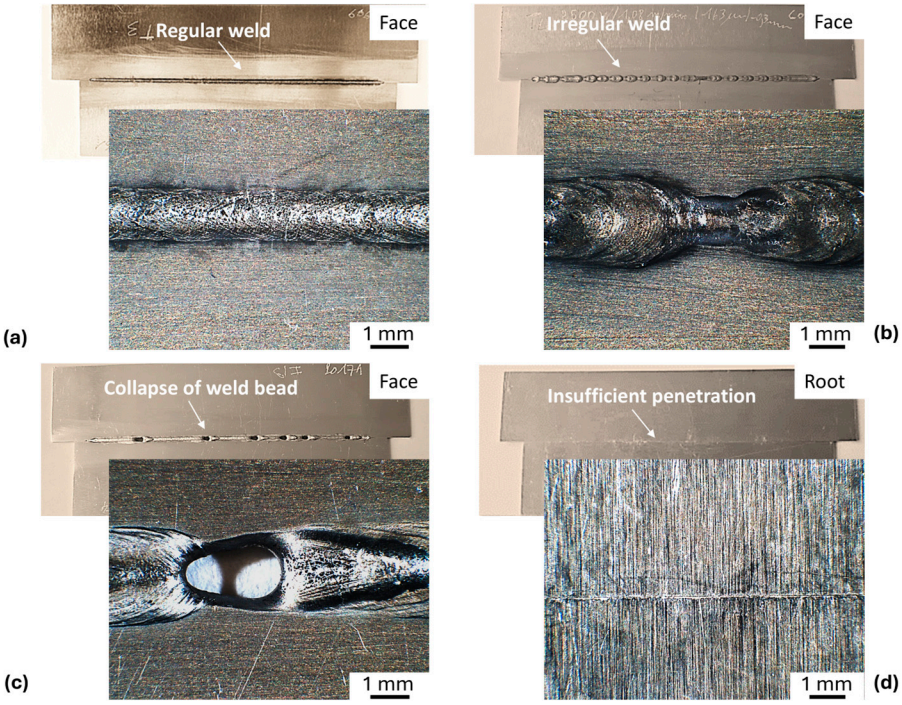

Figure 2. Examples of visual criteria used for weld quality assessment: (**a**) regular weld bead, (**b**) irregular weld bead, (**c**) collapse of the weld bead, and (**d**) insufficient penetration. Zoomed-in insets have been added to highlight key morphological features in each case, allowing for a more detailed visualization of typical defects and weld characteristics.

A scanning electron microscope (SEM) ZEISS GEMINI 1 coupled to an OXFORD X MAX energy dispersive spectrometer (EDS) is used to study the heat-affected zone (HAZ) and fusion zone (FZ) microstructure and defects such as cracks or porosity more thoroughly. Acceptable welds in the operating window are then tested in a tensile test using an INSTRON 5982 series testing machine at room temperature, with a constant crosshead speed of 1 mm·min^{-1}. These tests are carried out in the transverse direction of the sheets, and three samples are tested for each welding condition.

2.4. Hot Cracking Test

A crack susceptibility test based on the self-restraint cracking test is carried out on the aluminum alloys most susceptible to hot cracking [12]. This test consists of producing a fusion line on a trapezoidal specimen. The widths WF and WS of the trapezoidal plate are critical parameters for crack initiation and propagation, as they control the temperature gradient and, therefore, the thermal expansion of the melt pool in a perpendicular direction. The greater the width of WF and WS, the less severe the crack test. An optimized width WS of 20 mm and WF of 60 mm for a specimen length of 200 mm was suggested by Matsuda et al. for crack initiation in aluminum alloys.

Our experiment is carried out on a modified trapezoidal specimen [25], embedded at the broadest edge by a fixture specially designed for this study (Figure 3a). A fusion line of 150 mm in length (L_W) is made in the center of the specimen (Figure 3b). The length Lc of the hot crack is measured for each test by optical binoculars (Leica Wild M420) at ×32 magnification. A "critical width" (WC) is obtained at the width where crack propagation stops. Solidification crack susceptibility can be characterized by the crack length (Lc) or the ratio $\frac{L_C}{L_W}$ and the parameter WC. The longer the LC and WC, the higher the crack susceptibility. An argon flow of 20 L·min^{-1} and 10 L·min^{-1} protects the specimens' top and bottom from oxidation during laser welding (Figure 3c). Three specimens are tested for each welding condition.

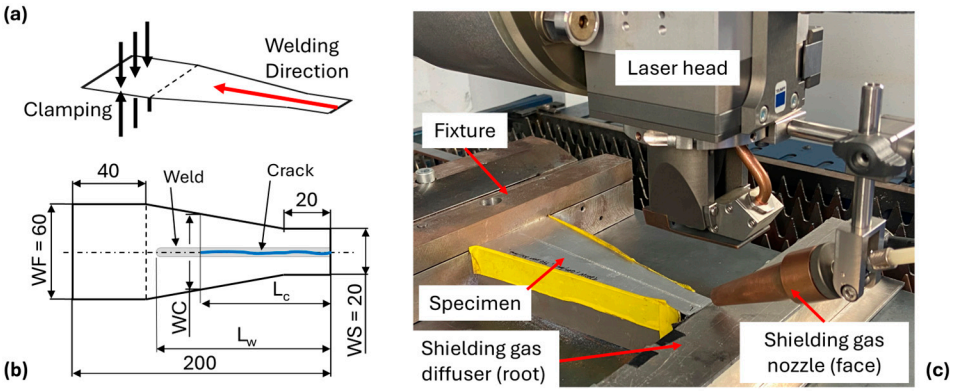

Figure 3. (**a**) Schematic representation of the trapezoidal sample; (**b**) specimen geometry [25], weld line location, and determination of the critical width of the WC; (**c**) configuration of the self-restraint cracking test.

3. Results

3.1. Process Window and Weld Quality

The results of the visual inspection of the weld joints are plotted as a function of laser power density and interaction time (Figure 4). This approach allows us to assess an essential process window for all aluminum alloys in a butt joint configuration.

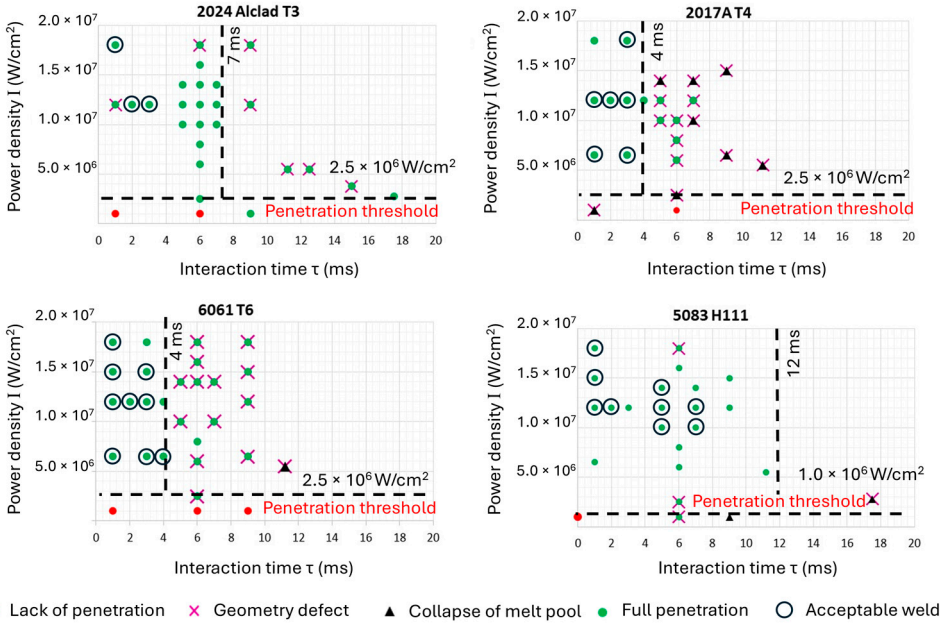

Figure 4. Laser welding process window according to weld penetration and weld aspect for the aluminum series, after visual inspection. Laser welding process window for aluminum alloys according to specified geometric criteria in the NF-L06-395-2010 standard (acceptable weld).

These graphs underline that a process window exists for all aluminum series. It is marked by two boundaries, which delimit approximately three domains: a domain with insufficient penetration, a domain with full penetration and regular weld, and another with irregular weld or cutoff. This first approach highlights an operating window that is significantly reduced in the case of AA2017 and AA6061 compared to AA2024 Alclad and AA5083 alloys. The threshold intensity for full penetration varies according to the aluminum alloy. A minimum power density of 2.5×10^6 W/cm^2 is required for AA2024 Alclad, AA2017, and AA6061, whereas it is twice as low for AA5083 alloys. This is mainly a function of power density and chemical composition. The high content of elements with a low boiling temperature, such as Si, Mn, Mg, and Zn, evaporates, favoring keyhole formation [26]. The difference in surface composition between AA2024 Alclad and the AA2017 alloy does not significantly affect the absorption of the laser beam. However, for the AA5083 alloy, a large amount of magnesium (4.0 to 4.9), compared to AA2024 Alclad, AA2017, and AA6061 alloys, appears to affect the penetration threshold density of the welds significantly. This can be explained by the lower boiling temperature of Mg than Al, favoring Mg vaporization and forming a deeper keyhole.

Regarding the influence of the interaction time, this parameter tends to favor weld irregularities and over-penetration in the power density range studied. In the case of the AA2017 and AA6061 series, irregular welds appear as early as 4 ms, whereas AA2024 Alclad and AA5083 are present at values two and three times higher, respectively. The weld densities are too high at high power densities and long interaction times, and the baths collapse. Optical examinations of the weld geometry are reported and plotted as a function of the power density and interaction time.

Preliminary welding tests are first carried out on AA2024 to evaluate the feasibility of different combinations of power density and interaction time. These trials reveal that certain parameter sets systematically result in welds with unacceptable geometrical defects, such as lack of fusion or excessive collapse, regardless of the energy density value. Consequently, these combinations are excluded from further testing. As a result, a higher number of energy density levels is presented for AA2024 in Figure 4. In contrast, only the most

promising and defect-free conditions are retained and applied to the other alloys. These standards are strictly adhered to, guiding the correct weld geometry. This phase allows us to obtain a weldability window, which underlines conditions that lead to an acceptable weld bead, ensuring the validity of the process. The width of the top and bottom welds does not meet the standard criteria and is the primary defect in the welds. Incorrect welds are wider than the maximum acceptable widths at the top and bottom. Other geometric defects, such as underfill or undercut, are not present. The weldability windows for AA2024 Alclad and AA2017 alloys are more reduced than for AA6061 and AA5083 alloys. An increase in interaction time up to 4 ms for 2024 and AA2017 alloys results in defective weld joints at the top and bottom. The interaction time is a limiting factor in obtaining an acceptable weld seam.

3.2. Effect of Energy Density on Weld Shape

The influence of energy density is investigated on AA2017, AA2024, AA5083, and AA6061 aluminum alloys. The welding bead width tends to increase with increasing energy density, which aligns with the results of Faye et al. [27] (Figure 5). A linear relationship between this parameter and the top weld width can be established. However, it should be noted that an increase in energy density does not have the same effect on bead width, according to the aluminum alloys. It can be observed that the smallest top weld widths are obtained with alloy AA5083.

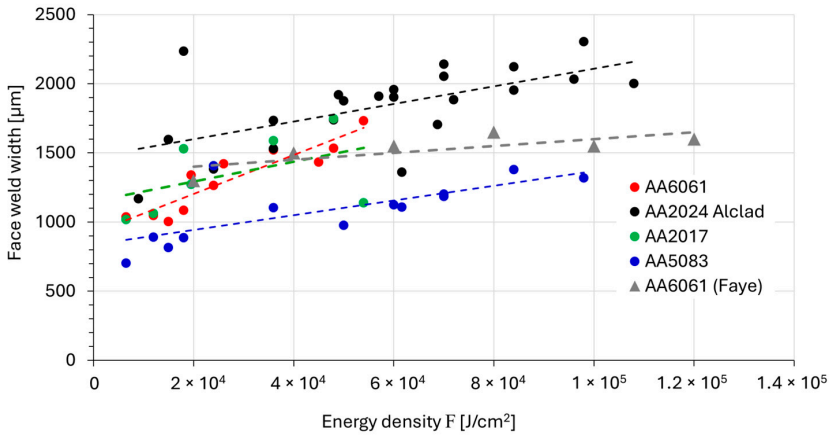

Figure 5. Influence of energy density on top weld width for AA2017, AA2024, AA5083, and AA6061.

While power density and energy density may appear conceptually similar, they are distinct physical parameters and should not be directly compared. Energy density reflects the total input per unit length, while power density characterizes the instantaneous concentration of energy on the surface. Nevertheless, in our experimental configuration, power density is strongly correlated with laser power, as the focal spot diameter remains relatively constant within a narrow range.

Our results (Figure 6) show that the interaction time has a more pronounced effect than power density on the top weld width. This observation suggests that the duration of energy input—rather than its instantaneous intensity—is a dominant factor in controlling heat conduction perpendicular to the welding direction. This is in agreement with the work of Ahn et al. [16], who reported similar behavior. The role of interaction time is therefore critical in understanding and optimizing the weld bead geometry.

Optical observations after a metallographic cross-section (Figure 7) exhibit an "hourglass" morphology for all laser welds, typical of a stable keyhole mode [16]. This morphology tends to change from an "hourglass" shape to a large rectangular shape with increasing energy density. In addition, minor geometrical defects such as underfill and undercut are

present, which confirm a stable welding regime [16]. Equiaxed dendrites are visible in the center of the melted area, while in the peripheral zone, dendrites are columnar and oriented, following the thermal gradient during solidification.

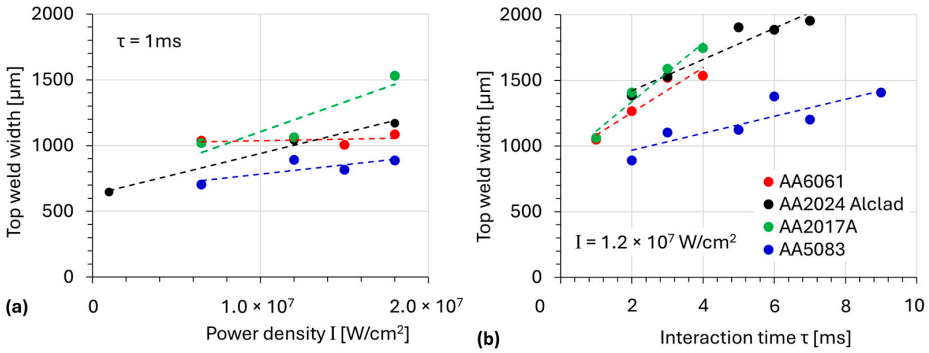

Figure 6. Influence of interaction time (**a**) and power density (**b**) on the face weld width for AA2017, AA2024 alclad, AA5083, and AA6061 aluminum alloys.

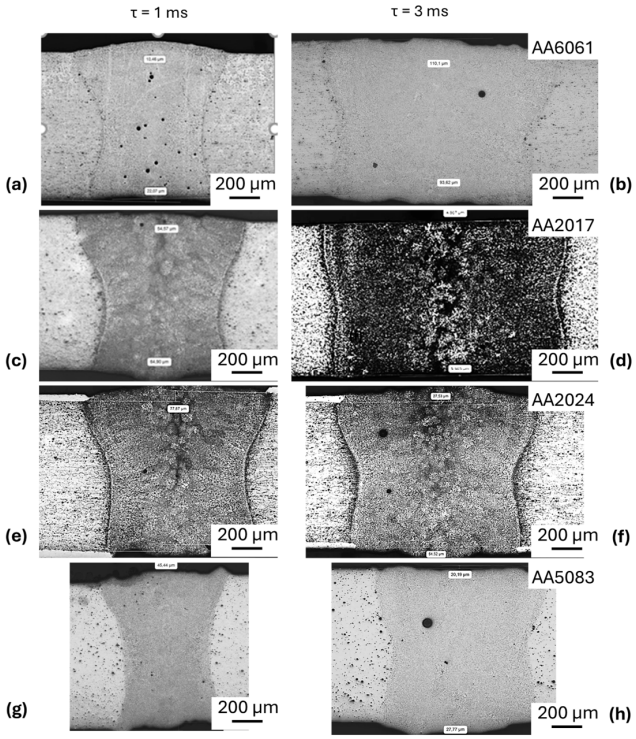

Figure 7. Evolution of the transverse cross-section of weld seams produced with given interaction times of 1 ms ((**a**), (**c**), (**e**), (**g**)) and 3 ms ((**b**), (**d**), (**f**), (**h**)) producing energy density of 1.2 × 10^4 and 3.6 × 10^4 J/cm^2, for welding of AA6061 (**a**) and (**b**), AA2017 (**c**) and (**d**), AA2024 (**e**) and (**f**), and AA5083 (**g**) and (**h**); Optical microscopy, Keller etching.

Some micro-voids are visible in the FZ, with an average diameter of 10–50 µm. ImageJ (version 1.54f), a free and open-source image processing software widely used in scientific analysis, is employed for the quantitative measurement of micro-voids. Their proportion, evaluated in a cross-section, is less than 1%. A few process porosities with a larger diameter in the 100–120 µm range are occasionally present. These round, regular-shaped micro-voids are characteristic of hydrogen discharge due to a drop in solubility during solidification [18,28]. The absence of coarse and irregular porosity confirms stable keyhole conditions for welds within the weldability window.

3.3. Microstructure and Microhardness of the Welded Joint

A metallographic cross-section highlights three distinct zones: base metal (BM), heat-affected zone (HAZ), and fusion zone (FZ) (Figure 8). A columnar dendritic structure marks the fusion line between the FZ and the HAZ, following the thermal gradient during solidification.

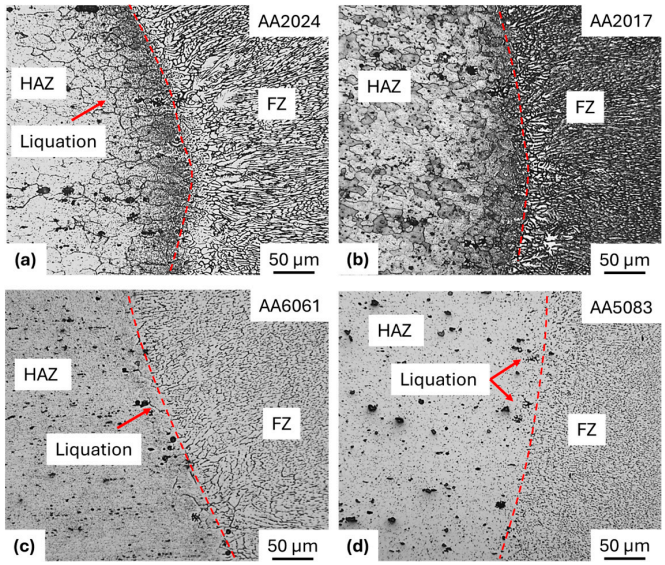

Figure 8. Examples of microstructure at the fusion line for acceptable welds obtained at 3.6×10^4 J/cm^2 (Keller etching) for (**a**) AA2024, (**b**) AA2027, (**c**) AA6061 and (**d**) AA6061 alloys.

Some coarse and dark particles are visible in the HAZ, with liquation at the fusion line, for the AA5083, AA6061, and 2024 series. This liquation is usually the starting point for solidification cracks [6,29].

The microstructure in the FZ shows a dendritic structure for AA2017 and AA2024 alloys and an equiaxed structure for AA5083 and AA6061 alloys with no solidification orientation (Figure 9). The presence of precipitates is not visible at this scale. A fast cooling rate characterizes the presence of fine dendrite arms in the FZ during welding [30]. For acceptable weld joints, the FZ must be free from cracking.

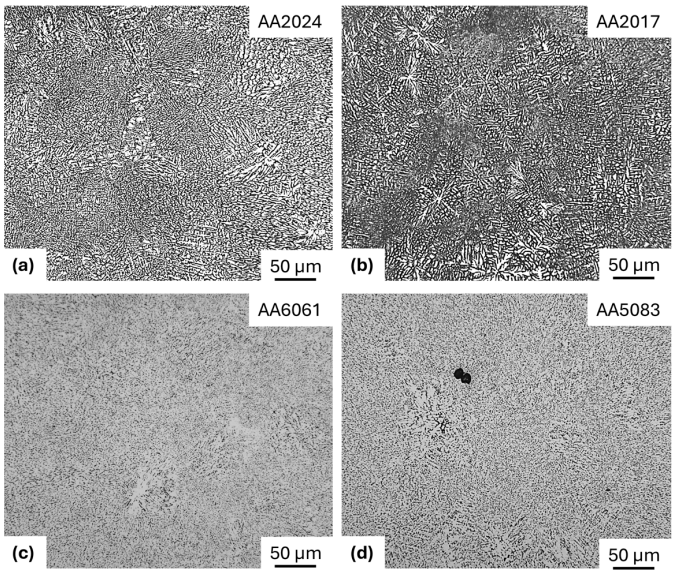

Figure 9. Example of dendritic microstructure in the FZ of the butt joints for acceptable welds obtained at 3.6×10^4 J/cm^2 (Keller etching), for (**a**) AA2024, (**b**) AA2027, (**c**) AA6061 and (**d**) AA6061 alloys.

3.4. Vaporization of Magnesium

Many studies have highlighted the evaporation of Mg for aluminum alloys [6,16,27,30] in the keyhole welding mode due to its low melting point and high vapor pressure. This loss of Mg degrades the mechanical properties and favors porosity [31].

In this part, two welding conditions are selected for energy dispersive X-ray (EDX) microanalysis to study the conditions for Mg vaporization. The first condition corresponds to an energy density at 1.2×10^4 J/cm^2 with 2500 W, 3.2 m/min^1, and a 163 µm beam diameter, and the second condition to an energy density three times higher at 3.6×104 J/cm^2 with 2500 W, 9.8 m/min^1, and a 163 µm beam diameter.

The average Mg content in the FZ welded specimens is measured on a cross-section (Figure 10b). There is no significant loss of Mg in the FZ on the welded specimens. Consequently, the fine porosity highlighted above could be attributed to hydrogen rejection in the melt zone due to the reduction in solubility. Nevertheless, a heterogeneous local repartition of Mg is visible in the FZ. It seems more pronounced in the sample welded at a higher energy density and lower welding speed.

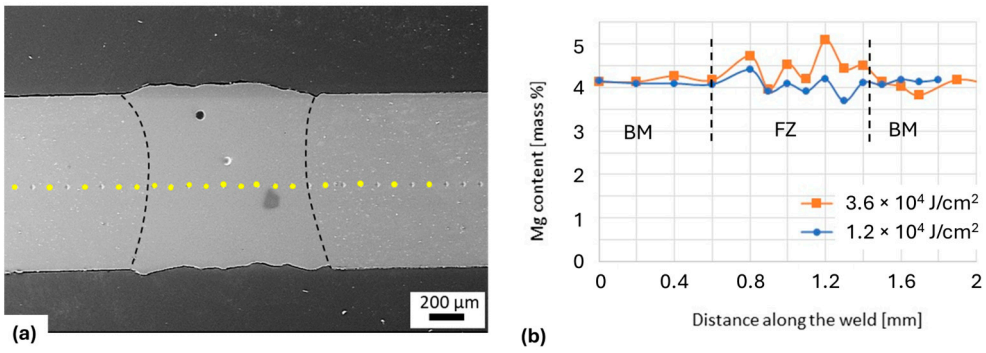

Figure 10. (**a**) Sites of interest for EDX analysis on a cross-section of welded samples, (**b**) Mg weight content across sample T1 welded at 3.6×10^4 J/cm^2 (2500 W, 3.2 m/min, 163 µm diam.), and sample T10 welded at 1.2×10^4 J/cm^2 (2500 W, 9.8 m/min, 163 µm diam.).

This may be related to chemical microsegregation due to the dendritic microstructure. On the other hand, the specimen, which is welded at a higher welding speed, shows a fine equiaxed dendritic structure (Figure 11). Welding speed is the first-order processing parameter that controls the heat input and, consequently, the evaporation of chemical elements and the cooling rate [16]. Although a keyhole mode risks vaporizing alloying elements, high-speed welding reduces the loss of Mg as the interaction time becomes shorter.

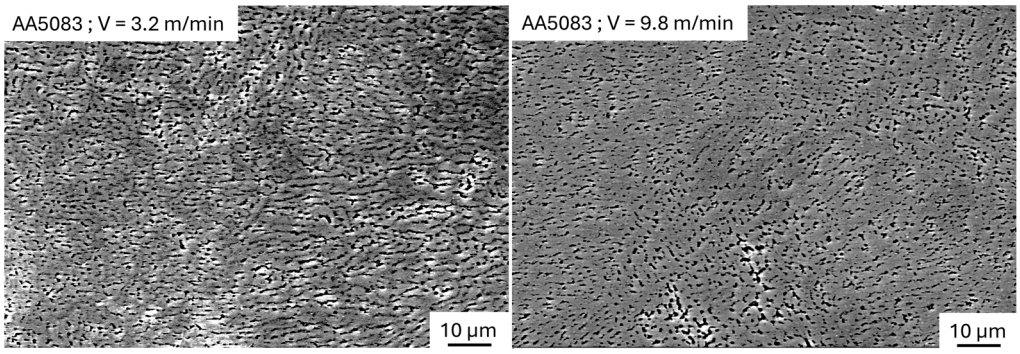

Figure 11. SEM observation of FZ microstructure: (**a**) columnar dendrites for the sample welded at 3.2 m/min, (**b**) equiaxed dendrites for the sample welded at 9.8 m/min.

The thermal effect of welding on the microstructure is measured using a ZWICK/ROELL-EMCO-Test microhardness tester in a transverse section in the center of the molten zone (Figure 12). These results show that the FZ's microhardness has a 30 to 50 HV drop for the AA2017, AA2024, and AA6061 alloys compared to the received sheets. On the contrary, an increase of around 10 HV for the AA5083 series can be noticed. A similar trend has been reported [1]. For the precipitation-hardening aluminum alloys AA2017, AA2024, and AA6061, this FZ softening can be explained by the dissolution of strengthening phases $AlCu_2$ or Mg_2Si, present at T3 or T4 temper for as-received sheets [16,23]. Concerning the slight increase in hardness for the AA5083 series, a possible explanation is a mechanical reinforcement because of the supersaturation of the solid solution combined with the formation of fine dendrites induced by a fast cooling rate [1,23].

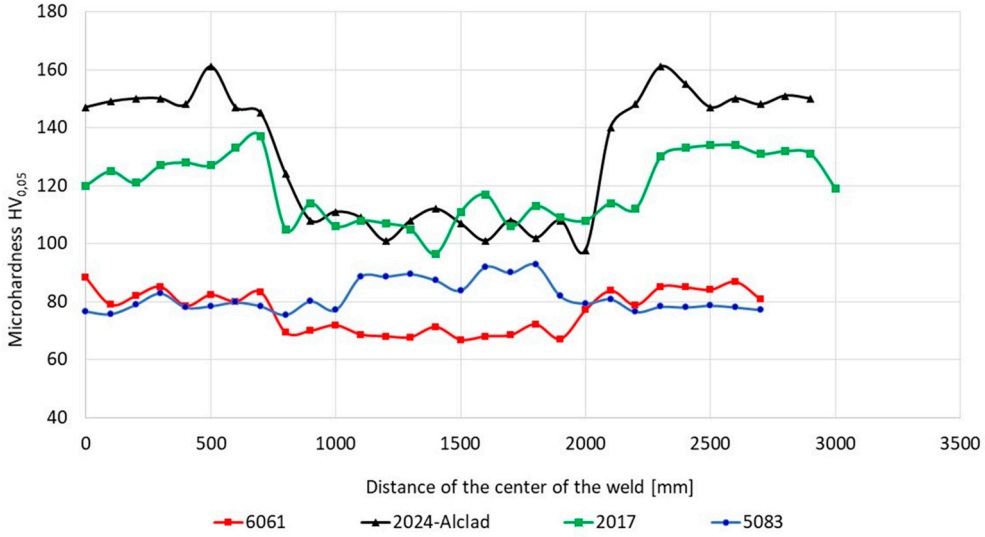

Figure 12. Microhardness profiles across acceptable welded joints at mid-thickness obtained with 3.6×10^4 J/cm^2.

As seen in Figure 12, the thermal effect of the weld is less pronounced in the HAZ than in the FZ for AA5083 and AA6061. Regarding the AA2024 and AA2017 alloys, the slight increase in HAZ hardness is around 20 points higher than in the BM. This could be explained by a re-precipitation of $AlCu_2$ hardening particles under the thermal effect after reaching the solution temperature.

3.5. Tensile Properties of Welded Joint

Tensile tests are only performed on acceptable full-penetration welds. Three samples are tested for each welding condition. Figure 13 shows that the fracture position of the laser welds seems to vary with energy density (Figure 13). For an energy density of 1.2×10^4 J/cm^2, the fracture of heat-treatable AA2024, AA2017, and AA6061 welded samples is located in the FZ, while for the non-heat-treatable AA5083 alloy, the fracture is located in the HAZ/BM.

Figure 14 shows the joint efficiencies for all aluminum alloys: the ratio of weld strength to base metal strength.

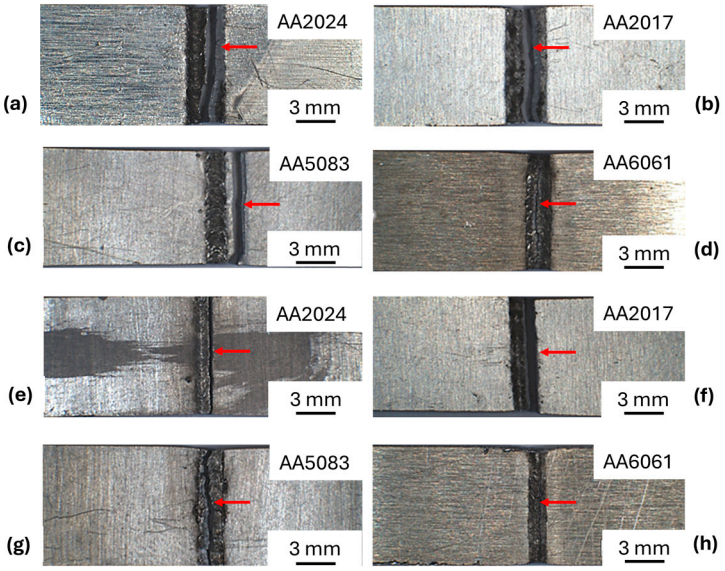

Figure 13. Fracture location after tensile tests of butt joints welded at (**a**–**d**) 1.2 × 10^4 J/cm^2 and (**e**–**h**) 3.6 × 10^4 J/cm^2.

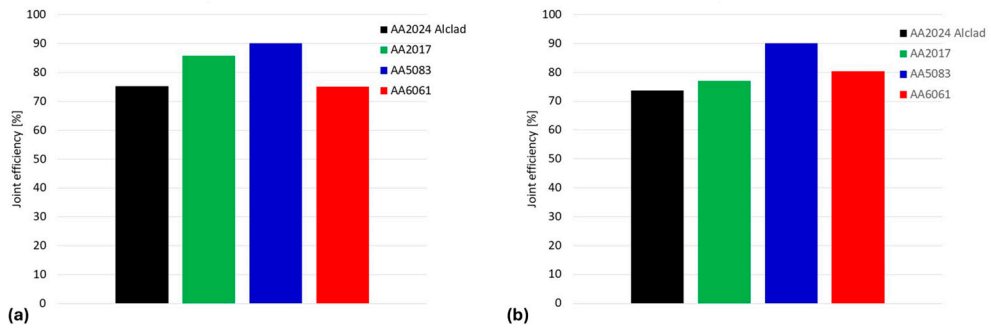

Figure 14. Joint efficiency of butt joints for AA2017, AA2024, AA5083, and AA6061 aluminum alloys as a function of energy density: (**a**) 1.2 × 10^4 J/cm^2 and (**b**) 3.6 × 10^4 J/cm^2.

Laser-welded joints of the AA5083 alloy appear to have the highest joint efficiency compared to the AA2024 Alclad, AA2017, and AA6061 alloys. The tensile strength of the AA5083 alloy is 90% of the base metal strength, while the tensile strength of the AA2024 Alclad, AA2017, and AA6061 alloys is between 85% and 75% of the base metal strength. Similar results using a conventional fiber and the Nd: YAG laser source were reported by Cao et al. [23]. An increase in energy density appears to slightly affect the AA2024 Alclad alloy's joint efficiency, which remains in the range of 60 to 80% of the base metal strengths, as reported by Cao et al. For the heat-treatable alloys AA2024 Alclad, AA2017, and AA6061, the reduction in tensile strength can be mainly attributed to the loss of hardening in the FZ and HAZ due to the dissolution of precipitate phases. In contrast, for the non-heat treatable alloy AA5083, the cause of this reduction in strength may be the loss of Mg [6] and the presence of porosity in the FZ.

The decrease in ductility is generally due to a cumulative effect between the microstructural change in the FZ, the orientation concerning the tensile solicitation, and the presence of defects such as porosities and defect geometries such as underfill and undercut [1,23]. This is believed to be due to the microstructural orientation and porosity in the weld bead for our welding conditions. On the other hand, an increase in energy density tends to reduce the ultimate tensile strength, with an improvement in elongation at break for all aluminum series. The tensile strength of the AA2024 alloy remains higher than that of the other alloys.

3.6. Hot Cracking Susceptibility

The susceptibility to hot cracking depends on many parameters, such as alloying (Mg, Si, Cu. . .), solidification temperature range, thermal conditions, types of joints, and fixture design. Thermal and solidification contraction can promote hot cracking by increasing external stress during cooling. Heat-treatable 2XXX and 6XXX aluminum alloys have a greater tendency toward hot cracking than work-hardening 5XXX alloys [12,23].

Consequently, a comparative study is conducted on the most sensitive AA2024 Alclad and 6061 alloys. Figure 15 shows the crack length of the tested specimens after the self-restraint cracking test as a function of the heat input. A red arrow marks the end of the crack as determined by optical binoculars.

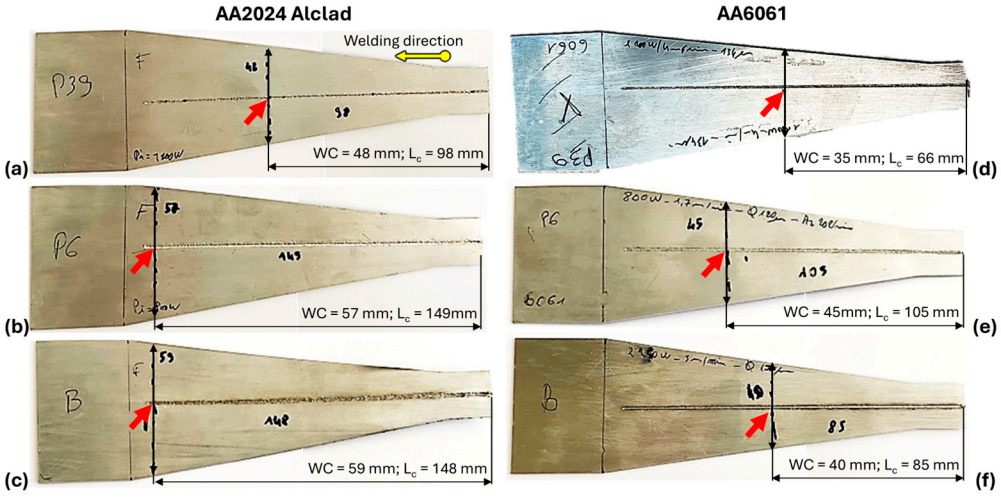

Figure 15. Macroscopic appearance of solidification cracking in AA2024 Alclad (**a**–**c**) and AA6061 (**d**–**f**) alloys with a WF and WS width of 20 mm and 60 mm, respectively, as a function of welding energy density.

Figure 16 shows details of the macroscopic morphology of the solidification cracks along the weld center. The crack in the center does not propagate in a straight line; it appears to follow the grain boundaries.

The hot crack propagation increases with the heat input due to more melted material and, consequently, more significant contraction (Figure 17a). These results agree with Ahn et al. [16]. The AA2024 Alclad alloy exhibits a higher propensity for crack formation than the AA6061 alloy (Figure 17b). Melting of the Alclad layer and its dilution in the weld bead do not appear to improve the crack susceptibility of the alloy. The 2024 alloy is twice as susceptible to cracking as the 6061 alloy. The thermal conductivity and solidification range of aluminum alloys have a significant influence on their susceptibility to hot cracking during laser welding. Alloys such as AA2024 and AA2017, which are precipitation-hardened and contain a relatively high amount of copper, exhibit lower thermal conductivity (~120–138 W/m·K) and wide solidification ranges (over 130 °C). These characteristics contribute to steep thermal gradients and a prolonged mushy zone during solidification, conditions that are known to favor hot cracking.

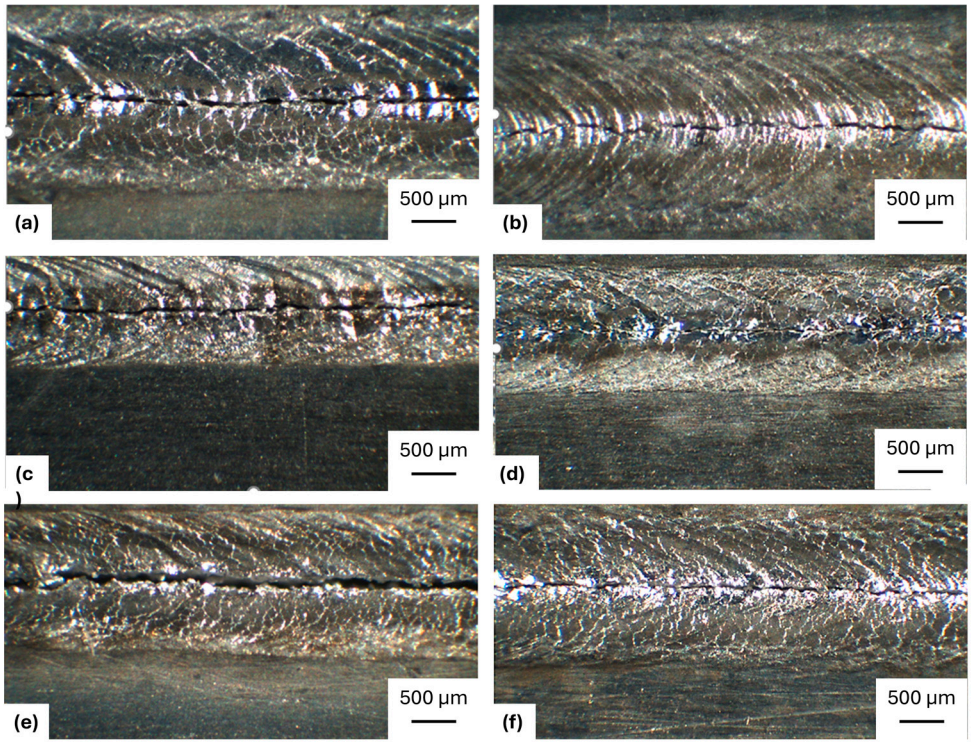

Figure 16. Details of the solidification crack in the horizontal plane of the weld joint. AA2024 alloy welded at 180 kJ·cm^{-1} (**a**), 280 kJ·cm^{-1} (**b**), and 458 kJ·cm^{-1} (**c**); AA6061 alloy welded at 180 kJ·cm^{-1} (**d**), 280 kJ·cm^{-1} (**e**), and 458 kJ·cm^{-1} (**f**).

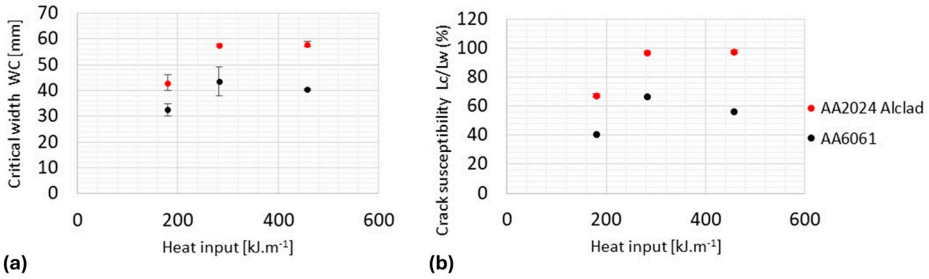

Figure 17. Comparison of the solidification crack susceptibility of AA2024 Alclad and AA6061 alloys as a function of heat input: (**a**) critical width WC, (**b**) $\frac{L_C}{L_W}$ ratio.

In contrast, AA6061 has a higher thermal conductivity (~167 W/m·K) and a narrower solidification range (~70 °C), which promote more uniform heat dissipation and reduce the duration of the partially solidified state. AA5083, a strain-hardened Al–Mg alloy, also shows relatively better behavior with respect to cracking, despite its lower thermal conductivity, due to the absence of low-melting eutectics typically found in Cu-containing alloys. These differences help explain the observed variations in hot cracking sensitivity among the studied alloys.

Metallographic examination of the crack formation at the top of the weld after polishing and chemical etching shows crack propagation at grain boundaries with different appearances (Figure 18). Cracks in alloy AA2024 propagate almost in a straight line and appear to follow the boundary of columnar grains, whereas in alloy AA6061, the sinuous propagation follows the contour of more equiaxed grains. A columnar microstructure is more prone to hot cracking than an equiaxed microstructure since it is more difficult for the liquid metal to maintain a uniform distribution [16,17]. The crack location and appearance of the AA2024 alloy remain unchanged with increasing heat input, as there is no significant

change despite a slight coalescence of the dendrites. In alloy AA6061, the cracks are more deflected due to the coalescence of the equiaxed grains.

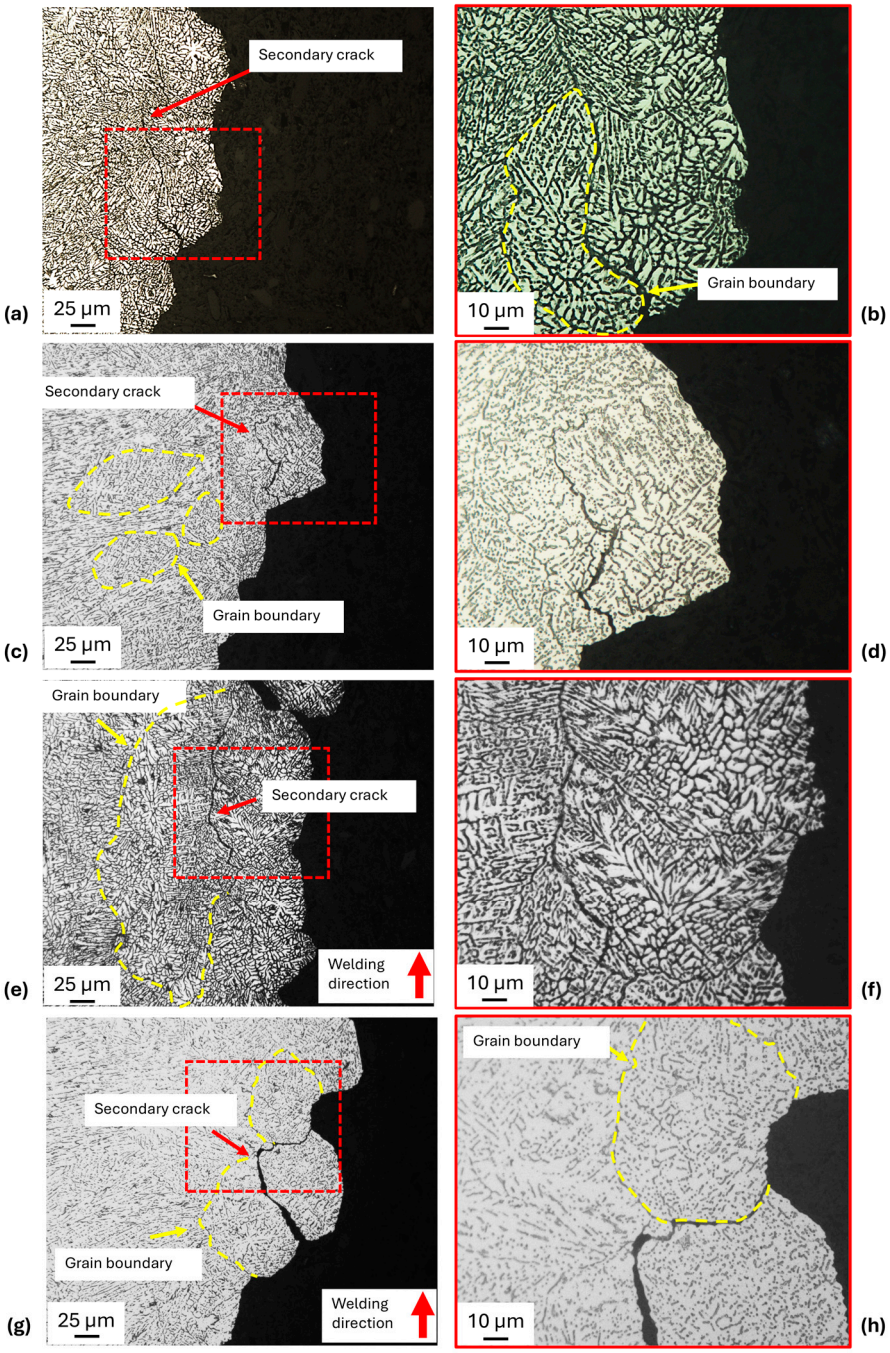

Figure 18. Relationship between hot crack propagation and microstructure of AA2024 and AA6061 alloys welded at (**a**–**d**) 180 kJ·m^{-1} and (**e**–**h**) 376 kJ·m^{-1}. General views ((**a**), (**c**), (**e**), (**g**)) and detailed cracked areas ((**b**), (**d**), (**f**), (**h**)).

SEM analysis of the fracture surface of the crack shows a smooth, intact dendritic appearance typical of solidification cracking (Figure 19). This aspect could indicate that the cracking occurs in a liquid phase at the final stage. The presence of some granular areas (yellow arrows) for AA6061 alloys could be attributed to a ductility crack due to partial film solidification.

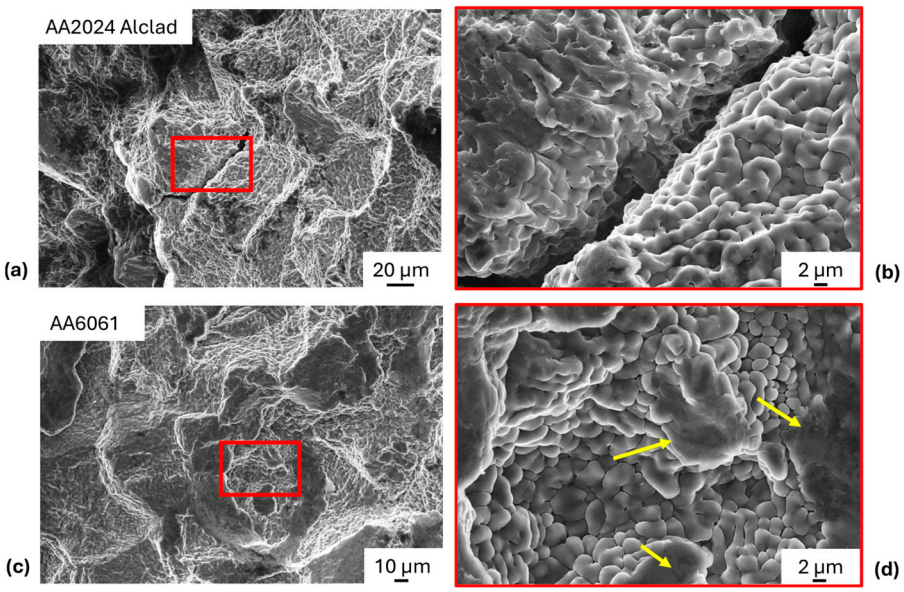

Figure 19. Characteristics of the surface of solidification cracks in AA2024 ((**a**), (**b**)) and AA6061 ((**c**), (**d**)) alloys welded at 180 kJ·cm^{-1}; general ((**a**) and (**c**)) and detailed views ((**b**) and (**d**)). Yellow arrows point granular fracture surface.

4. Conclusions

This study has demonstrated the possibility of obtaining a weldability window for laser keyhole welding of 1.2 mm-thick aluminum alloys of AA2024 Alclad, AA2017, AA6061, and AA5083 series using a Yb: YAG laser disc. The following conclusions were reached:

1. The power density parameter controls the weld penetration, while the interaction time controls the weld geometry. Optimizing these parameters favors keyhole stability and reduces defects such as porosity, weld geometry, and hot cracking.
2. For the AA2024 Alclad and AA2017 aluminum series, a columnar dendritic structure is observed in the FZ for welds in the weldability window. In contrast, for the AA5083 and AA6061 alloys, morphology is essentially equiaxed dendritic. A liquation phenomenon at the fusion line between the FZ and HAZ is present for all welds in the weldability window.
3. The Vickers hardness values over the whole cross-section associated with this microstructure are shallow in the FZ compared to the BM for heat-treatable aluminum alloys. This is a consequence of the dissolution of the strengthening phase. In the case of the non-heat treatable alloy AA5083, a slight increase in hardness is observed, probably due to solid solution supersaturation and microstructural refinement.
4. Tensile strength and elongation after fracture of welded specimens are lower than the BM for all aluminum series. The fracture of the welded joints is located at the FZ or the FZ/HAZ line. Laser welds of AA5083 alloy have the highest joint efficiency compared to the AA2017, AA2024 Alclad, and AA6061 alloys.
5. A self-restraint crack test on the hotter crack-sensitive alloys AA2024 Alclad and AA6061 shows that the crack length increases with increasing heat input for both aluminum alloys. However, the crack sensitivity of the AA2024 Alclad alloy appears to be higher than that of the AA6061 alloy, probably due to the presence of a columnar dendritic structure, which favors crack propagation.

Author Contributions: Conceptualization, J.-D.B., Y.B. and J.A.; methodology, J.-D.B., Y.B. and J.A.; validation, J.-D.B., Y.B. and J.A.; formal analysis, J.-D.B. and Y.B.; investigation, J.-D.B., J.P. and N.A.; data curation, J.-D.B. and Y.B.; writing—original draft preparation, J.-D.B.; writing—review and editing, J.-D.B., Y.B. and J.A.; visualization, J.-D.B. and Y.B.; supervision, Y.B. and J.A.; project administration, Y.B. and J.A.; funding acquisition, J.A. All authors have read and agreed to the published version of the manuscript.

Funding: This research received no external funding.

Data Availability Statement: The raw data supporting the conclusions of this article will be made available by the authors on request.

Conflicts of Interest: The authors declare no conflicts of interest. The funders had no role in the design of the study; the collection, analysis, or interpretation of data; the writing of the manuscript; or the decision to publish the results.

References

1. Pang, X.; Dai, J.; Chen, S.; Zhang, M. Microstructure and Mechanical Properties of Fiber Laser Welding of Aluminum Alloy with Beam Oscillation. *Appl. Sci.* **2019**, *9*, 5096. [CrossRef]
2. Vyskoč, M.; Sahul, M.; Dománková, M.; Jurči, P.; Sahul, M.; Vyskočová, M.; Martinkovič, M. The Effect of Process Parameters on the Microstructure and Mechanical Properties of AW5083 Aluminum Laser Weld Joints. *Metals* **2020**, *10*, 1443. [CrossRef]
3. Bunaziv, I.; Akselsen, O.M.; Ren, X.; Nyhus, B.; Eriksson, M. Laser Beam and Laser-Arc Hybrid Welding of Aluminium Alloys. *Metals* **2021**, *11*, 1150. [CrossRef]
4. Rajendran, C.; Ben Ruben, R.; Ashokavarthanan, P.; Mallieswaran, K. Identifying the Effect of PWHT on Strength of Laser Beam Welding Joints of AA2024 Aluminum Alloy. *ASME Open J. Eng.* **2022**, *1*, 011003. [CrossRef]
5. Ramiarison, H.; Barka, N.; Amira, S. Optimization of Parameters in Laser Welding of Aluminum Alloy 5052-H32 Using Beam Oscillation Technique for Mechanical Performance Improvement. *Int. J. Lightweight Mater. Manuf.* **2022**, *5*, 470–483. [CrossRef]
6. Cao, X.; Wallace, W.; Immarigeon, J.-P.; Poon, C. Research and Progress in Laser Welding of Wrought Aluminum Alloys. II. Metallurgical Microstructures, Defects, and Mechanical Properties. *Mater. Manuf. Process.* **2003**, *18*, 23–49. [CrossRef]
7. Garavaglia, M.; Demir, A.G.; Zarini, S.; Victor, B.M.; Previtali, B. Process Development and Coaxial Sensing in Fiber Laser Welding of 5754 Al-Alloy. *J. Laser Appl.* **2019**, *31*, 022419. [CrossRef]
8. Deepak, J.R.; Anirudh, R.P.; Saran Sundar, S. Applications of Lasers in Industries and Laser Welding: A Review. *Mater. Today Proc.* **2023**, S221478532300620X. [CrossRef]
9. Deng, A.; Chen, H.; Zhang, Y.; Liu, Y.; Yang, X.; Zhang, Z.; Zhang, B.; He, D. Prediction of the Influence of Welding Metal Composition on Solidification Cracking of Laser Welded Aluminum Alloy. *Mater. Today Commun.* **2023**, *35*, 105556. [CrossRef]
10. Ghaini, F.M.; Sheikhi, M.; Torkamany, M.J.; Sabbaghzadeh, J. The Relation between Liquation and Solidification Cracks in Pulsed Laser Welding of 2024 Aluminium Alloy. *Mater. Sci. Eng. A* **2009**, *519*, 167–171. [CrossRef]
11. Dittrich, D.; Keßler, B.; Strohbach, R.; Jahn, A. Laser Beam Welding of Hot Crack Sensitive Al-Alloys without Filler Wire by Intensity Controlled Dynamic Beam Oscillation. *Procedia CIRP* **2022**, *111*, 435–438. [CrossRef]
12. Löveborn, D.; Larsson, J.K.; Persson, K.-A. Weldability of Aluminium Alloys for Automotive Applications. *Phys. Procedia* **2017**, *89*, 89–99. [CrossRef]
13. Wang, J.; Wang, H.-P.; Wang, X.; Cui, H.; Lu, F. Statistical Analysis of Process Parameters to Eliminate Hot Cracking of Fiber Laser Welded Aluminum Alloy. *Opt. Laser Technol.* **2015**, *66*, 15–21. [CrossRef]
14. Abioye, T.E.; Mustar, N.; Zuhailawati, H.; Suhaina, I. Prediction of the Tensile Strength of Aluminium Alloy 5052-H32 Fibre Laser Weldments Using Regression Analysis. *Int. J. Adv. Manuf. Technol.* **2019**, *102*, 1951–1962. [CrossRef]
15. Demirorer, M.; Suder, W.; Ganguly, S.; Hogg, S.; Naeem, H. Development of Laser Welding of High Strength Aluminium Alloy 2024-T4 with Controlled Thermal Cycle. *MATEC Web Conf.* **2020**, *326*, 08005. [CrossRef]
16. Ahn, J.; Chen, L.; He, E.; Dear, J.P.; Davies, C.M. Optimisation of Process Parameters and Weld Shape of High Power Yb-Fibre Laser Welded 2024-T3 Aluminium Alloy. *J. Manuf. Process.* **2018**, *34*, 70–85. [CrossRef]
17. Hekmatjou, H.; Naffakh-Moosavy, H. Hot Cracking in Pulsed Nd:YAG Laser Welding of AA5456. *Opt. Laser Technol.* **2018**, *103*, 22–32. [CrossRef]
18. Hou, J.; Li, R.; Xu, C.; Li, T.; Shi, Z. A Comparative Study on Microstructure and Properties of Pulsed Laser Welding and Continuous Laser Welding of Al-25Si-4Cu-Mg High Silicon Aluminum Alloy. *J. Manuf. Process.* **2021**, *68*, 657–667. [CrossRef]
19. Rasch, M.; Roider, C.; Kohl, S.; Strauß, J.; Maurer, N.; Nagulin, K.Y.; Schmidt, M. Shaped Laser Beam Profiles for Heat Conduction Welding of Aluminium-Copper Alloys. *Opt. Lasers Eng.* **2019**, *115*, 179–189. [CrossRef]

20. Punzel, E.; Hugger, F.; Dinkelbach, T.; Bürger, A. Influence of Power Distribution on Weld Seam Quality and Geometry in Laser Beam Welding of Aluminum Alloys. *Procedia CIRP* **2020**, *94*, 601–604. [CrossRef]
21. Davis, J.R. Introduction to Aluminum and Aluminum Alloys. In *Metals Handbook Desk Edition*; ASM International: Materials Park, OH, USA, 1998; pp. 417–423, ISBN 978-1-62708-199-3.
22. Mondolfo, L.F. Aluminum–Magnesium, Aluminum–Manganese Alloys. In *Aluminum Alloys*; Elsevier: Amsterdam, The Netherlands, 1976; pp. 806–841, ISBN 978-0-408-70932-3.
23. Cao, X.; Wallace, W.; Poon, C.; Immarigeon, J.-P. Research and Progress in Laser Welding of Wrought Aluminum Alloys. I. Laser Welding Processes. *Mater. Manuf. Process.* **2003**, *18*, 1–22. [CrossRef]
24. Bouffier, L. Modélisation de La Fissuration à Chaud Lors Du Soudage de l'alliage Base Nickel IN600. Ph.D. Thesis, Université de Grenoble, Grenoble, France, 2013.
25. Miyagi, M.; Wang, H.; Yoshida, R.; Kawahito, Y.; Kawakami, H.; Shoubu, T. Effect of Alloy Element on Weld Pool Dynamics in Laser Welding of Aluminum Alloys. *Sci. Rep.* **2018**, *8*, 12944. [CrossRef]
26. Faye, A.; Balcaen, Y.; Lacroix, L.; Alexis, J. Effects of Welding Parameters on the Microstructure and Mechanical Properties of the AA6061 Aluminium Alloy Joined by a Yb: YAG Laser Beam. *J. Adv. Join. Process.* **2021**, *3*, 100047. [CrossRef]
27. Alfieria, V.; Caiazzoa, F.; Sergi, V. Autogenous Laser Welding of AA 2024 Aluminium Alloy: Process Issues and Bead Features. *Procedia CIRP* **2015**, *33*, 406–411. [CrossRef]
28. Zhang, P.; Jia, Z.; Yu, Z.; Shi, H.; Li, S.; Wu, D.; Yan, H.; Ye, X.; Chen, J.; Wang, F.; et al. A Review on the Effect of Laser Pulse Shaping on the Microstructure and Hot Cracking Behavior in the Welding of Alloys. *Opt. Laser Technol.* **2021**, *140*, 107094. [CrossRef]
29. Qin, L.; Du, W.; Cipiccia, S.; Bodey, A.J.; Rau, C.; Mi, J. Synchrotron X-Ray Operando Study and Multiphysics Modelling of the Solidification Dynamics of Intermetallic Phases under Electromagnetic Pulses. *Acta Mater.* **2024**, *265*, 119593. [CrossRef]
30. Ion, J.C. Laser Beam Welding of Wrought Aluminium Alloys. *Sci. Technol. Weld. Join.* **2000**, *5*, 265–276. [CrossRef]
31. El-Batahgy, A.; Kutsuna, M. Laser Beam Welding of AA5052, AA5083, and AA6061 Aluminum Alloys. *Adv. Mater. Sci. Eng.* **2009**, *2009*, 974182. [CrossRef]